mater.scichina.com link.springer.com

Published online 17 February 2023 | https://doi.org/10.1007/s40843-022-2317-0
Sci China Mater 2023, 66(5): 2013–2022

2D-3D perovskite memristor with low energy consumption and high stability for neural morphology calculation

Kaixuan Sun[1], Qingrui Wang[2], Long Zhou[2], Jingjuan Wang[1], Jingjing Chang[2], Rui Guo[3*], Beng Kang Tay[3,4*] and Xiaobing Yan[1*]

ABSTRACT **Recently, rapid progress has been made in the application of organic-inorganic halide perovskites in electronic devices, such as memristors and artificial synaptic devices. Organic-inorganic halide perovskite is considered as a promising candidate for the next generation of computing devices due to its ion migration property and advantages in manufacturing. In this work, a two-dimensional (2D)-3D organic-inorganic hybrid perovskite memristor was studied, using the stacking structure of indium tin oxide (ITO)/$FA_{1-y}MA_yPbI_{3-x}Cl_x$/$(PEA)_2PbI_4$/Au. The results show that this new type of memristor has novel resistance switching characteristics, such as scanning-rate-dependent current switching property, good current-voltage (*I-V*) curve repeatability, and ultralow energy consumption. A defect-modulated electron tunneling mechanism is demonstrated using the p-i-n junction model, and it is proven that the conductance state of the memristive device is determined by the defect concentration in the perovskite film near the electrode sides. In addition to the good memristive properties, this 2D-3D perovskite memristor can also function well as an artificial synapse, and its internal defect movement can faithfully simulate the inflow and extrusion of Ca^{2+} in biological synapses. Moreover, this perovskite-based artificial synapse has ultra-low power consumption due to the switchable p-i-n structure in organic-inorganic halide perovskites. Our finding highlights the immense application potential of the 2D-3D perovskite memristor in the future neuromorphic computing system.**

Keywords: perovskite, ion migration, memristor, low energy consumption, neuromorphic computing

INTRODUCTION

ABX_3 is a general formula for organic-inorganic halide perovskites, where A represents organic cations (e.g., methyl ammonium ($CH_3NH_3^+$, MA^+) and formamidine ($CH[NH_2]_2^+$, FA^+)) or inorganic compounds (e.g., K^+, Rb^+, and CS^+), B represents divalent metal cations (e.g., Pb^{2+} and Sn^{2+}), and X represents halides (X = Cl^-, Br^-, and I^-) [1,2]. In recent years, organic-inorganic halide perovskites have been widely studied in photovoltaic devices due to their significant optical and electronic properties [3–5]. The organic-inorganic halide perovskites have unique properties rarely seen in other materials: (I) tunable band gap [6–8], (II) majority carrier control [9,10], (III) fast ion migration [11–13], and (IV) super flexibility [14–16], which therefore attracts researchers' attention. Besides, recently, organic-inorganic halide perovskites have been applied in other optoelectronic devices, including light-emitting diodes, X-ray detectors, and energy converters [17]. More recently, rapid progress has been made in the application of organic-inorganic halide perovskites in other electronic devices, such as resistance switching memory, field effect transistors (FET), and artificial synaptic devices [18]. It is expected that in the near future, organic-inorganic halide perovskites will become an important active and semiconductor material for the next generation of computing devices. The conductivity change of organic-inorganic halide perovskite-based solar cells has been shown in the process of rapid development. However, currently, a substantial explanation for the memristive mechanism of ion migration-based perovskite memristors is still lacking. For example, Meloni *et al.* [19] attributed the hysteresis phenomenon in organic-inorganic halide perovskites to charge migration, which is supported by the first principle simulations. Walsh *et al.* [6] proposed that halide ions migrate more easily than organic cations as their energy of defect formation is smaller than that of the latter. Although long-term migration of ions/defects of organic-inorganic halide perovskites is an obstacle in perovskite solar cells, this behavior may extend their application to migration-related memristors. Moreover, the characteristics of organic-inorganic halide perovskites can be tailored [20] by changing the composition of organic-inorganic halide perovskites by adding various substitute elements [8] and defect engineering [9]. Current-voltage (*I-V*) hysteresis and forward/reverse scan currents due to rapid ion migration can be utilized in memristors and artificial synaptic devices, in which high power amplifiers are used for non-optoelectronic applications. In this work, the memristive mechanism of organic-inorganic halide perovskite devices will be discussed in detail.

Conventional perovskite memristors are usually based on the conductive filament mechanism, which have the disadvantages

[1] Key Laboratory of Brain-like Neuromorphic Devices and Systems of Hebei Province, College of Electron and Information Engineering, Hebei University, Baoding 071002, China
[2] State Key Discipline Laboratory of Wide Band Gap Semiconductor Technology, School of Microelectronics, Xidian University, Xi'an 710071, China
[3] Centre for Micro- and Nano-Electronics (CMNE), School of Electrical and Electronic Engineering, Nanyang Technological University, Singapore 639798, Singapore
[4] UMI 3288 CINTRA (CNRS-NTU-THALES Research Alliances), Nanyang Technological University, Singapore 637553, Singapore
[*] Corresponding authors (emails: arenaguo@gmail.com (Guo R); EBKTay@ntu.edu.sg (Tay BK); yanxiaobing@ime.ac.cn (Yan X))

of high energy consumption and instability. Besides, a variety of unique electrical properties of perovskite materials are ignored in these memristors. In this work, we demonstrate a two-dimensional (2D)-3D memristor based on an organic-inorganic halide perovskite. Interestingly, the memristor shows novel resistive switching behaviors, of which the current switching is dependent on the scanning rate. A defect-modulated electron tunneling mechanism is demonstrated using the p-i-n junction model, and it proves that the conductance state of the memristive device is determined by the defect concentration near the film/electrode interface. Moreover, the 2D-3D memristor also displays excellent synaptic learning characteristics with the advantage of ultralow energy consumption, which is due to the p-i-n structure. With the detailed discussion of the mechanism, our results provide important guiding reference for the application of organic-inorganic halide perovskite materials in the future neuromorphic computing system.

EXPERIMENTAL SECTION

Device fabrication

Methylammonium iodide (MAI, 99.9%, Alfa aesar), formamidinium iodide (FAI, 99.9%, Alfa aesar), lead iodide (PbI_2, 99.9%, sigma), lead chloride ($PbCl_2$, 99.9%, sigma), poly(3,4-ethylenedioxythiophene):polystyrene sulfonate (PEDOT:PSS, Baytron-p 4083), and 2-phenylethylamine hydroiodide (PEAI, 98.0%, TCI) were used in this study. 2D/3D perovskite films based on 3D $MA_{1-y}FA_yPbI_{3-x}Cl_x$ were prepared by spin coating process. The detailed experimental process is shown in Fig. S1. In order to deposit 2D/3D perovskite hybrid films on indium tin oxide (ITO), perovskite precursor solution was prepared. PbI_2 and $PbCl_2$ were dissolved and stirred at 65°C for 12 h. Then 100 mg of 7:3 MAI and FAI were dissolved in isopropyl alcohol (IPA). PbI_2 and $PbCl_2$ solutions (1.36 and 0.24 mol L^{-1}) were spin-coated at 3000 r min^{-1} for 45 s, and then MAI solution was spin coated on the top of the dried PbI_2 layer and annealed at 100°C for 10 min. MAI (1 mg) and PEAI (2 mg) solutions dissolved in IPA (1 mL) were spin coated on perovskite films, and annealed at 100°C for 5 min. ITO glass substrate (10 Ω sq^{-1}) was ultrasonically cleaned with deionized water, acetone and ethanol for 20 min, and then dried with nitrogen. Then, the ITO substrate was treated with ultraviolet (UV) ozone for 20 min to remove the organic residue. Perovskite thin film was spin coated on ITO as the absorption layer. Finally, the gold top electrode with a thickness of 100 nm was prepared on the perovskite surface by electron beam evaporation (temescalfc-2000). The effective area of all devices is 0.07 cm^2.

Device characterizations

The surface and cross section images were obtained by field emission scanning electron microscopy (FESEM, JSM-7600F, JEOL). The crystal structure was characterized by grazing incidence-X-ray diffraction (GI-XRD, D8 advance, Bruker) and XRD (SmartLab, RIGAKU). XRD data were recorded in the 2θ range of 5°–60° with a scanning speed of 6° min^{-1}. The UV-visible (UV-Vis) absorption spectra were measured by a Perkin Elmer lambda 950 spectrophotometer. Photoluminescence (PL) and time-resolved PL (TR-PL) spectra were recorded by picosecond fluorescence time 300 under the action of a 510-nm picosecond pulse laser. X-ray photoelectron spectroscopy (XPS) measurements were performed on Escalb250Xi, and the source was monochromatic alka (1486.6 eV). Electrical performance was recorded by a digital source meter (Agilent B1500A). The decay process of hysteresis current and voltage was recorded by a digital oscilloscope (LeCroy WaveSufer 62XMS-B).

RESULTS AND DISCUSSION

Characterization results and electrical measurements

SEM was conducted to reveal the microscopic structure of the perovskite film. As shown in Fig. 1a, the thickness of perovskite film is about 500 nm. The SEM image also obviously reveals the 2D/3D feature of the perovskite film, which is due to the steric hindrance effect of PEA^+ and the formation of benzene ring π. In addition, the diffusion of PEA^+ cations to grain boundaries leads to the formation of 2D perovskite films, which makes the surface morphology become rough (Fig. 1b) [21,22]. It is obvious that layered 2D perovskite ($(PEA)_2PbI_4$) exists on 3D perovskite ($MA_{1-y}FA_yPbI_{3-x}Cl_x$) grains, and excessive PbI_2 reacts with MAI/PEAI to form 2D perovskite, which further passivates the grain boundaries. The formation of 2D phase was also verified by the atomic force microscopy (AFM) measurements. As shown in Fig. 1c, the thickness of the step is about 3 nm determined according to the line profile of 2D perovskite. XRD was carried out to test the structure of 2D/3D perovskite. There is no peak shift in the XRD pattern of perovskite thin film, which indicates that the crystal structure of 3D perovskite has not changed despite the incorporation of 2D perovskite. Besides, a small peak appears at about 565 nm, consistent with the band gap of quasi 2D perovskite, suggesting the formation of 2D perovskite (Fig. S2a, b). Similar results were observed in UV-Vis spectroscopy, as shown in Fig. S3a, which can further verify the formation of 2D/3D hybrid perovskite. Organic inorganic halide perovskite thin films have a variety of defects (trap states), which have been widely studied. The more trapped states in perovskite films, the shorter the PL decay recombination lifetime. TR-PL decay measurements were performed to estimate the recombination lifetime of 2D/3D hybrid perovskite films deposited on glass substrates (Fig. S3b). The results show that there are more defects (trap states) in our films compared with the literature (Table S1). This can be explained by the different preparation conditions (annealing time and temperature in the deposition process), which have a significant effect on the trapped states. It is worth noting that the average lifetime of carriers in the 2D/3D perovskite treated by PEAI is significantly longer than that of the original 3D perovskite. The XPS spectrum (Fig. S4) of the mixed 2D/3D perovskite film displays the characteristic peaks of both 3D and 2D perovskites, signifying the creation of 2D/3D perovskite heterostructures. Meanwhile, the reduction of work function can be verified by the measurement of Kelvin probe force microscopy (KPFM). Obviously, the surface potential of 3D perovskite film is significantly different from that of 2D-3D perovskite film (Fig. S5). Electrical measurements were carried out to test the *I-V* properties of the devices with the structures shown in Fig. 1d. Typical *I-V* switching curves are displayed in Fig. 1e. Different from the conventional oxide-based memristor, the *I-V* curves of the devices used in this study are relatively smooth, showing bidirectional resistance switching characteristics, without the phenomenon of current mutation. The switching voltage (1.0, −0.5 V) is very small, and the 200 cycles of *I-V* characteristic curves overlap with only slight change in the negative voltage scanning phase, which shows excellent

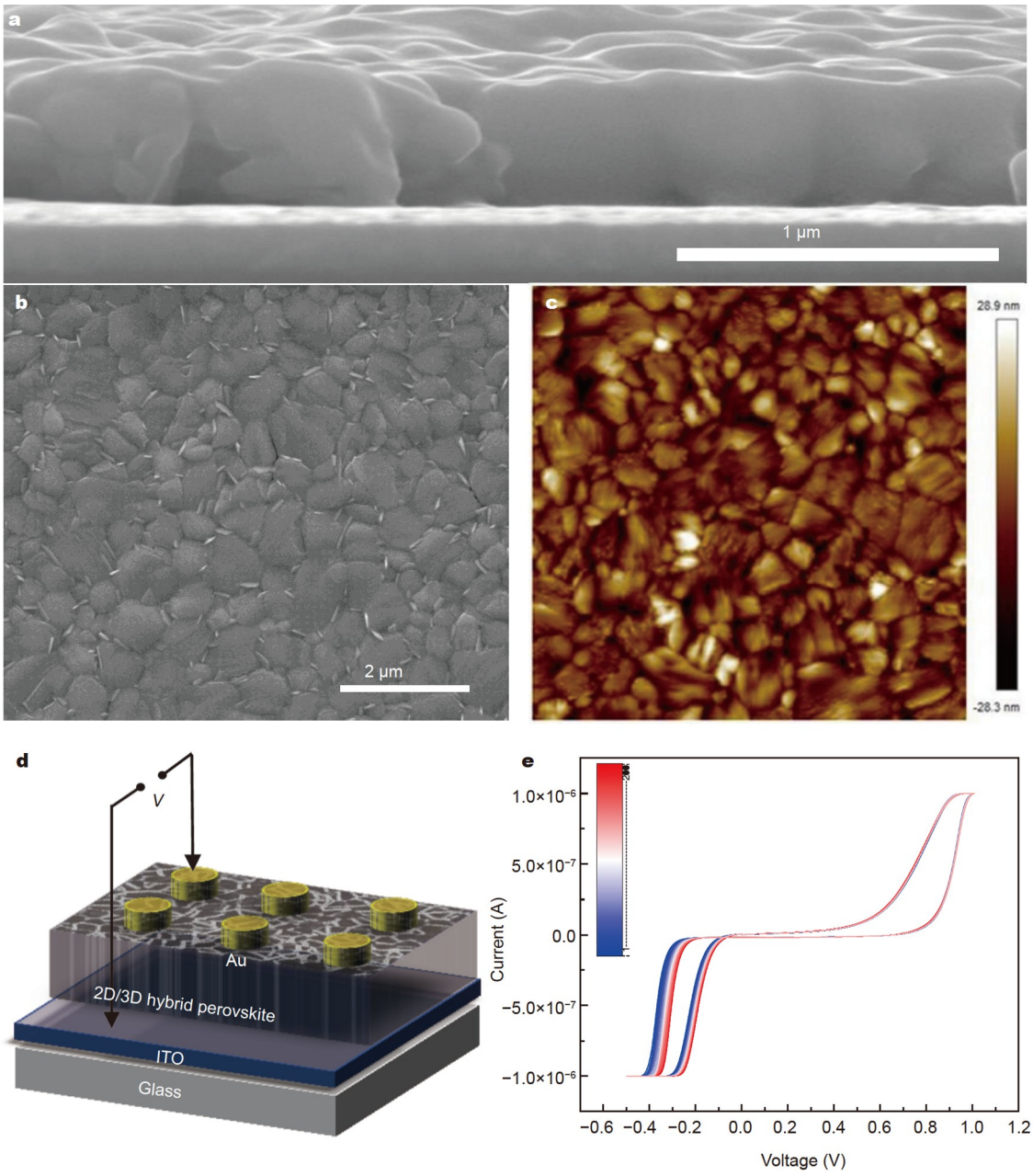

Figure 1 SEM images of the perovskite film $(PEA)_2PbI_4/MA_{1-y}FA_yPbI_{3-x}Cl_x$: (a) cross-section image, (b) surface morphology. (c) AFM image of the 2D/3D perovskites film. (d) Schematic of the vertical structure of ITO/2D/3D perovskite/Au. (e) 200 cycles of *I-V* characteristics of the ITO/2D/3D perovskite/Au device.

repeatability of the device.

I-V curves of the ITO/2D/3D perovskite/Au devices were tested with different scanning rates, from 200 to 1000 mV s^{-1}. In order to further explore the influence of the scanning rate on *I-V* curves, a series of electrical tests were carried out, as shown in Fig. 2. The devices show different *I-V* characteristic curves at different scanning rates, as shown in Fig. 2a, which has not been reported before. The high and low conductivity values at different scanning rates of 200 cycles were measured as shown in Fig. 2c. The conductance value of low-resistance state (LRS) at different scanning rates is almost unchanged, around 10 μS, with no obvious fluctuation. With the increase of scanning rate from 200 to 1000 mV s^{-1}, the conductance value of high-resistance state (HRS) also increases gradually from 0.018 to 0.101 μS (Fig. 2c), without obvious fluctuation. Moreover, the scanning-rate-dependent resistance switching phenomenon is observed. An additional 200 cycles of *I-V* scanning curves (50 cycles for each type of current limiting) were measured for the open limiting current, and the limiting current was set to 1, 3, 5 and 7 μA, as shown in Fig. 2d. The shape of *I-V* curves under different current limiting conditions is basically unchanged, and the scanning within 200 cycles almost coincides, which indicates that the change of limiting current will not affect the stability of the device. Note that, in the process of *I-V* scanning, there is no formation of the *I-V* switching process and stable conductance state of this device, which is different from the memristor based on the filament mechanism. As shown in Fig. 2b, the *I-V* characteristic curve does not pass through the origin point. This

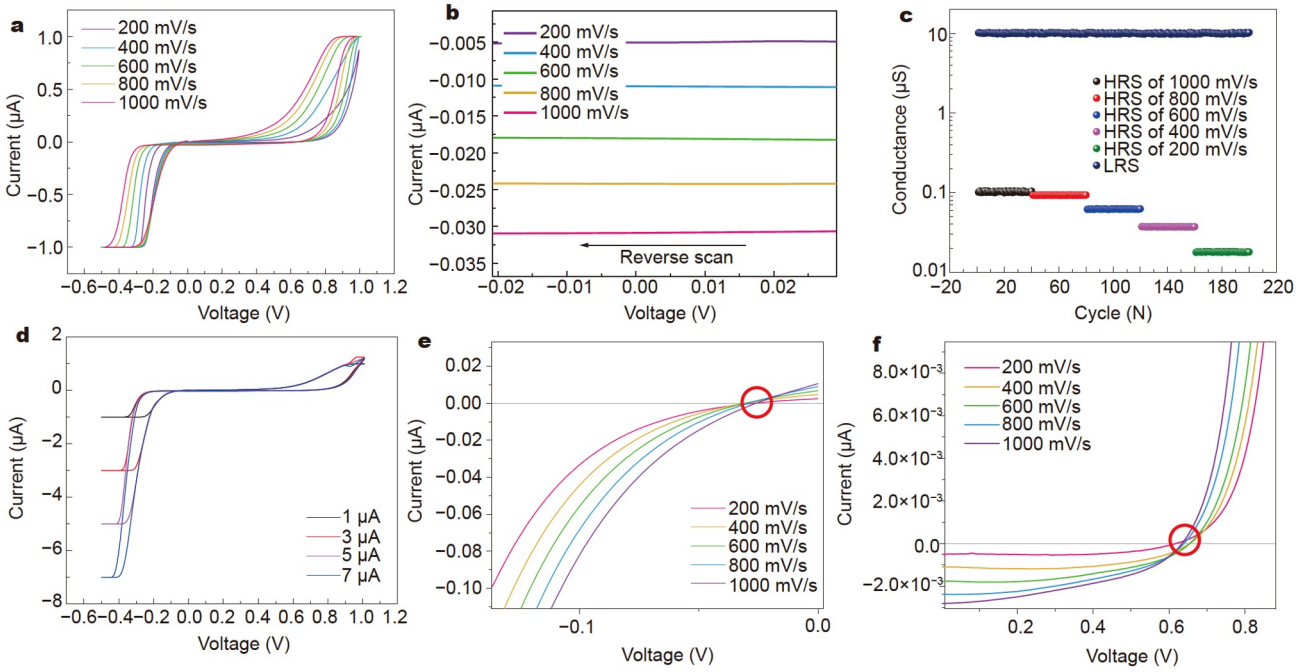

Figure 2 (a) *I-V* cycle curves of the ITO/2D/3D perovskite/Au devices at scanning rates of 200, 400, 600, 800 and 1000 mV s^{-1}, respectively. (b) Comparison of the hysteresis currents around 0 V for reverse scanning at different scanning rates. (c) Conductivity distribution of LRS and HRS of the ITO/ 2D/3D perovskite/Au devices at scanning rates of 200, 400, 600, 800 and 1000 mV s^{-1}, respectively. (d) *I-V* curves of ITO/2D/3D perovskite/Au devices under an compliance current (I_{CC}) at 1, 3, 5 and 7 μA, respectively. (e) V_{oc} in the backward scanning at different scanning rates. (f) V_{oc} in the forward scanning at different scanning rates.

kind of hysteresis current has not been reported in memristors with various resistance switching mechanisms, but observed in solar cell devices based on organic-inorganic hybrid halide perovskites. The studies of charge transport and conductivity of organic-inorganic hybrid halide perovskites mainly focus on their semiconductor (electron/hole transport) behavior, and show high carrier mobility and long minority carrier diffusion length [23]. The *I-V* characteristics show that the current lags behind the voltage [20], which is presumed to be related to ion migration [24]. Xing *et al.* [25] proposed that the non radiative pathways involved in electron hole recombination may include bulk defects such as vacancies. According to the spectral impedance study, Dualeh *et al.* [26] proposed that in addition to electron conduction, ion charge transfer may also exist in hybrid perovskites. In addition to ion migration, ferroelectric is also considered as possible mechanisms [20]. Recent studies of quasi elastic neutron scattering data [12] and piezoelectric response force microscopy (PFM) measurements [27] indicate that the ferroelectricity in $CH_3NH_3PbI_3$ is unlikely to be the main mechanism behind the observed hysteresis phenomenon. The research results of Tress *et al.* [24] have shown that light has no direct effect on the switching hysteresis in current of organic-inorganic halide perovskites. In order to reveal the origin of the rate-dependent resistance switching characteristics in ITO/2D/3D perovskite/Au devices, two possible mechanisms which may explain the memristive behaviors in organic-inorganic hybrid perovskite devices are discussed: the ferroelectricity of perovskite films, and the movement and accumulation of ions/defects leading to the doping effect. In order to study the ferroelectric properties of 2D-3D perovskite films, PFM was conducted, as shown in Fig. S6. Although a much higher bias voltage than the coercive voltage is applied, the PFM amplitude and phase signals are very weak, and the polarization direction cannot be switched after ±8 V bias voltage is applied. The local hysteresis switching loop cannot be obtained either. Therefore, the ferroelectric effect should be eliminated in this study.

Mechanism discussion

As discussed above, the resistive switching of the devices is dependent on the scanning rate. Moreover, it is found that the scanning rate affects not only the HRS, LRS, and switching voltage of the device, but also the hysteresis current, as shown in Fig. 2b. Specifically, the hysteresis current increases with the increase of scanning rates, and the value of hysteresis current is approximately proportional to the scanning rate. Therefore, it is speculated that the nature of hysteresis current may be capacitive current. The open circuit voltage (V_{OC}) of forward scanning and backward scanning are basically the same under different scanning rates (Fig. 2e, f). It has been reported that similar halide-containing perovskites are good halide ion vacancy conductors at high temperatures [12]. First principle calculations have been used to study the halide perovskite [28]. Defect studies show that the vacancies of Pb^{2+}, I^-, Cl^-, MA^+ and FA^+ produce shallow levels [9,29]. The recent simulation work [30] shows the universality of ion over electron disorder in $FA_{1-y}MA_yPbI_{3-x}Cl_x$, and the formation energy of Schottky defects related to vacancies is low, as shown in the following reaction using Kröger-Vink symbol to represent all Schottky defects,

$$Nil = V_{MA}' + V_{FA}' + V_{Pb}'' + 3(V_I^{\bullet} + V_{Cl}^{\bullet}) + FA_{1-y}MA_yPbI_{3-x}Cl_x,$$

where Nil represents the perfect $FA_{1-y}MA_yPbI_{3-x}Cl_x$ lattice, V represents the vacancy, the subscript represents the ion type and the superscript represents the effective defect charge (one point for each positive charge and one prime for each negative charge).

Recent results [29] show that the significant equilibrium concentration of positive and negative vacancies supports vacancy-mediated diffusion.

It is theoretically predicted that the negatively charged Pb, MA and FA vacancies (V_{MA}', V_{FA}' and V_{Pb}") will lead to p-type doping, while the positively charged I and Cl vacancies ($V_I^{\bullet}$, $V_{Cl}^{\bullet}$) will lead to n-type doping in perovskite films. These vacancies all act as unintentional doping sources [9,30]. In this case, the electric field makes the charged vacancy with low energy in $FA_{1-y}MA_yPbI_{3-x}Cl_x$ drift near the electrode to form a p-i-n structure. Taking the vertical structure device as an example, our resistance switching scheme is shown in Fig. 3a, b. In the process of forward bias, positively charged ions or vacancies move to and accumulate on the ITO electrode side, resulting in n-type doping in perovskite on the ITO electrode side. Similarly, the remaining negative space charge layer can be p-type doped with the perovskite layer to make it close to the side of Au electrode. The perovskite film in the middle is used as the intrinsic layer to form the p-i-n homogeneous junction structure. Reverse bias can switch the structure of p-i-n to n-i-p by forcing ions or ion vacancies to drift in the opposite direction. The memristive current and hysteresis current can also be explained by the time-varying drift of ions in the field [31]. The blue arrow indicates the direction of the built-in electric field. Due to the existence of the built-in electric field, there will be a potential difference between the perovskite films. Therefore, it is speculated that the hysteresis current is caused by the strong internal electric field generated by the electric dipole in the n-type region and the p-type region. In this model, because the built-in potential competes with the applied bias voltage, the size of the built-in potential will be reflected in the V_{OC} of the reverse scanning, and the size of the built-in potential should be determined by the maximum value of the applied bias voltage. Therefore, although the magnitude of the hysteresis current depends on the scanning rate, when the same bias voltage is applied, the magnitude of V_{OC} is little affected by the scanning rate, as shown in Fig. 2e, f.

Due to the rectification characteristics of the *I-V* curve of ITO/2D/3D perovskite/Au devices, it is speculated that there is a Schottky barrier at the interface between the metal and semiconductor. *I-V* curves were fitted to verify the electron transport mechanism, and the results show that direct tunneling and Fowler-Nordheim (F-N) tunneling are the main electron transmission modes in the device (Fig. S7a). When the applied bias approaches the barrier height, these mechanisms compete, resulting in a transition from logarithmic growth to linear attenuation. This transition corresponds to the voltage required to change the barrier shape from trapezoid to triangle. In this study, this special applied bias threshold is called transition voltage, or V_{trans}. However, due to the rectification characteristics of *I-V* curves of ITO/2D-3D perovskite/Au devices, it is speculated that there is a Schottky barrier at the interface between the metal and semiconductor, as described above. The structure of p-i-n junction of ITO/2D-3D perovskite/Au device is therefore confirmed. Therefore, in the process of forward bias, the moving ions and holes will form a p-type space charge region at the interface between the perovskite film and Au electrode, resulting in the downward bending of energy band. At the same time, an n-type space charge region is formed at the interface between the perovskite film and ITO electrode, resulting in the upward bending of energy band. Therefore, with the increase of scanning voltage, the charge accumulates continuously, and the bending degree of energy band increases gradually, resulting in the increase of the potential barrier height φ. According to Equation S4, during F-N tunneling, the current curve between ln(I/V^2) and $1/V$ will produce a line, and its slope will depend on the barrier height φ. Due to the increasing barrier height, the slope of the curve between ln(I/V^2) and $1/V$ should also increase to a certain extent. As shown in Fig. S7b, during F-N tunneling, the slope also increases with the increase of voltage, which also supports the hypothesis of p-i-n junction model. Furthermore, with the increase of interface doping concentration, there will be an approximate ohmic contact between the electrode and perovskite film, resulting in a further reduction of resistance.

The curves of ln(I/V^2) and $1/V$ of devices under different scanning rates are shown in Fig. 3c. It is found that the resistance switching mechanisms under different scanning rates are the same. Only V_{trans} increases slightly with the increase of scanning rate in the process of negative scanning. Fig. 3d shows the curves of ln($|I|/V^2$) and $1/|V|$ of the device under different scanning rates in the negative bias scanning stage. It is obvious that during the transition from direct tunneling to F-N tunneling, with the increase of scanning rate, the turning point $1/V$ increases, corresponding to V_{trans} decreases. The p-i-n junction model is used to explain this phenomenon. Since the scanning process from positive bias to negative bias is continuous and there is reverse current under zero bias, there is still capacitance effect at the interface at the beginning of negative scanning. Therefore, there is still accumulation of ions and vacancies at the interface on both sides of perovskite film, as shown in Fig. 3e. State I shows the energy band diagram of the interface at zero bias; at this stage, negatively charged ions and holes gather on the Au side, bending the energy band downward. Due to the influence of negative bias voltage, the positively charged holes and ions begin to move to the Au electrode, and the negatively charged holes and particles start to move to ITO. The equilibrium state is reached at a certain time as shown in state II; at this stage, the main conductive mechanism is still direct tunneling. Later, due to the application of negative voltage, the holes and ions begin to move and gather at the corresponding side of the perovskite film. Finally, in state III, the conduction mechanism changes from direct tunneling to F-N tunneling. This also explains the slight drift of the *I-V* curve under negative bias in Fig. 1e. The potential generated by positive bias is stronger than that generated by negative bias in each cycle, which is reflected in the increase of V_{trans} under negative bias.

Neural calculation

In order to improve the stability of the device and adjust the symmetry of the hysteresis loop of the device, PEDOT:PSS is covered on ITO as the bottom electrode as the work functions of PEDOT:PSS and Au electrodes are almost the same (Fig. S8a). The curve shows bidirectional switching characteristics under continuous bias scanning. It can be seen that after PEDOT:PSS layer is added, V_{trans} can be modulated to about 0.15 V, which can lower the power consumption. Besides, the uniformity, stability and symmetry of the device are greatly increased. Specifically, the device obtains relatively symmetrical current response under symmetrical bias voltage, and the change of limiting current will not affect the *I-V* characteristic curve of the device (Fig. S8b). Perovskite synapses have a variety of biological functions, including peak time-dependent plasticity (STDP), peak rate-dependent plasticity (SRDP), and short-term plasticity

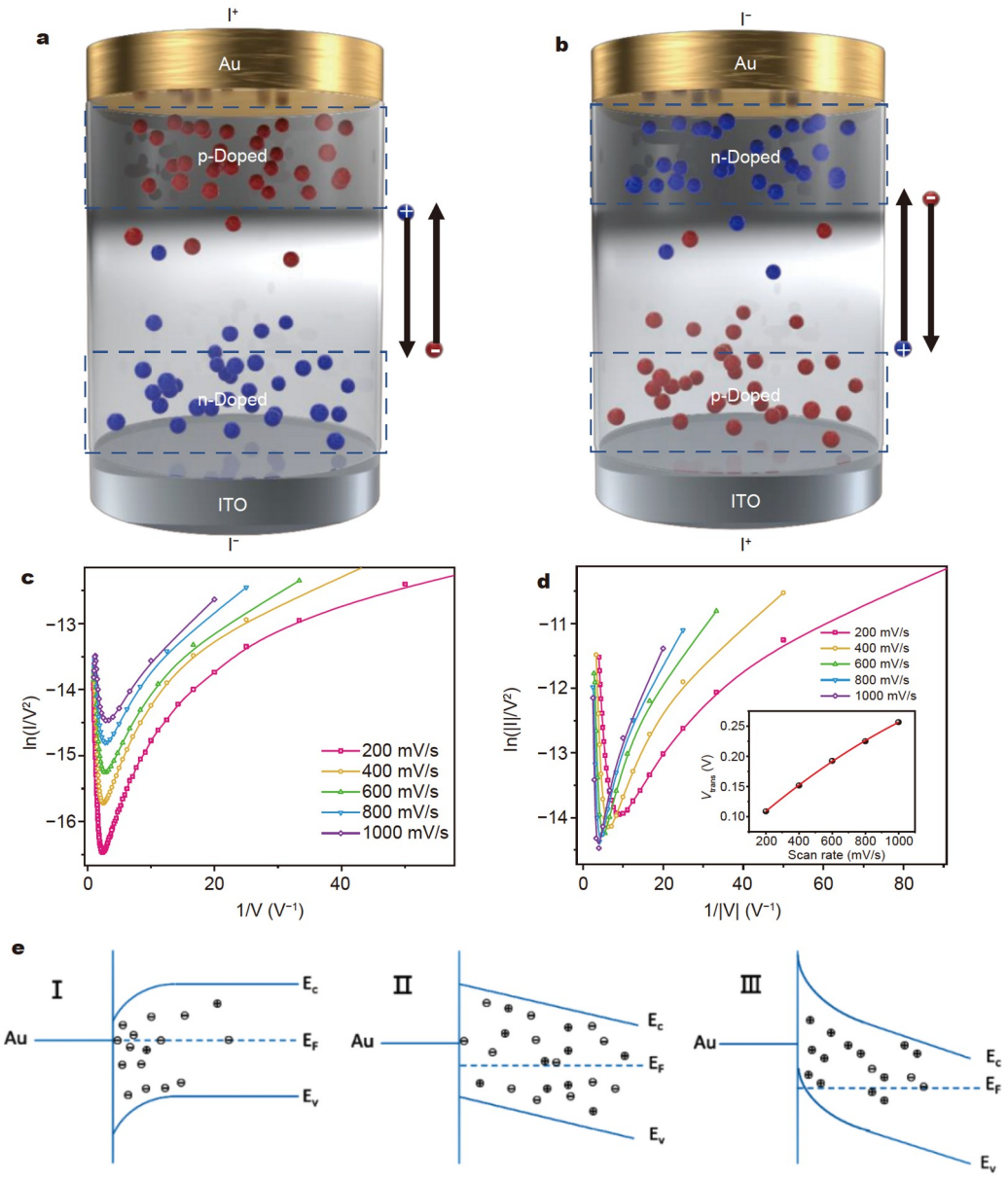

Figure 3 (a) Schematic diagrams of ion drift in perovskite during positive bias and (b) negative bias show that the ions accumulated in perovskite close to the electrode induce p-type and n-type doping, respectively. (c) Curves of $\ln(I/V^2)$ and $1/V$ at different scanning rates under forward bias, corresponding to direct tunneling and F-N tunneling, respectively. (d) Curves of $\ln(|I|/V^2)$ and $1/|V|$ at different scanning rates under negative bias correspond to direct tunneling and F-N tunneling, respectively. The illustration shows the change of V_{trans} with scanning rate. (e) Energy band diagrams of three states of interface between the Au electrode and 2D-3D perovskite under reverse bias. State I: zero bias, state II: the bias increases, and state III: the bias is close to V_{trans}.

(STP). As shown in Fig. S9a, when a continuous negative spike (0 to −0.3 V) scan is applied to the device, the amplitude of the current continues to increase. This indicates that defect concentration on both sides of the device is increasing, and the device is in the p-i-n state at this stage. As shown in Fig. S9b, when a continuous positive bias (0 to 0.3 V) is applied to the device, the current and conductivity values continue to increase, indicating that defect diffuses in the opposite direction and gradually switches the device to p-i-n polarity. The results show that due to the formation of p-i-n structure, the shift of Fermi level is beneficial to the generation of memristive behavior, which is consistent with the former report [32]. By applying a series of spike pulses, the conductance/resistance of the device can also be gradually adjusted, which is a typical behavior of memristor.

Fig. 4a shows an applied pulsed current with a fixed amplitude of ±0.48 V and a reading pulse of −0.1 V. The negative and positive spikes result in the opposite movement and accumulation of defects in the device, which leads to the reversal of p-i-n and n-i-p junctions of the device. The conductance of the device can be repeatedly tuned more than 500 times. Among the ten states measured in Fig. 4b, the conductivity of each state fluctuates between 3.4% and 8.6%. Besides, the ion migration in perovskite films can faithfully mimic the infiltration and extrusion of Ca^{2+} in presynaptic membranes, as shown in Fig. 4c. An important function of synapse is STDP [33–36], which means

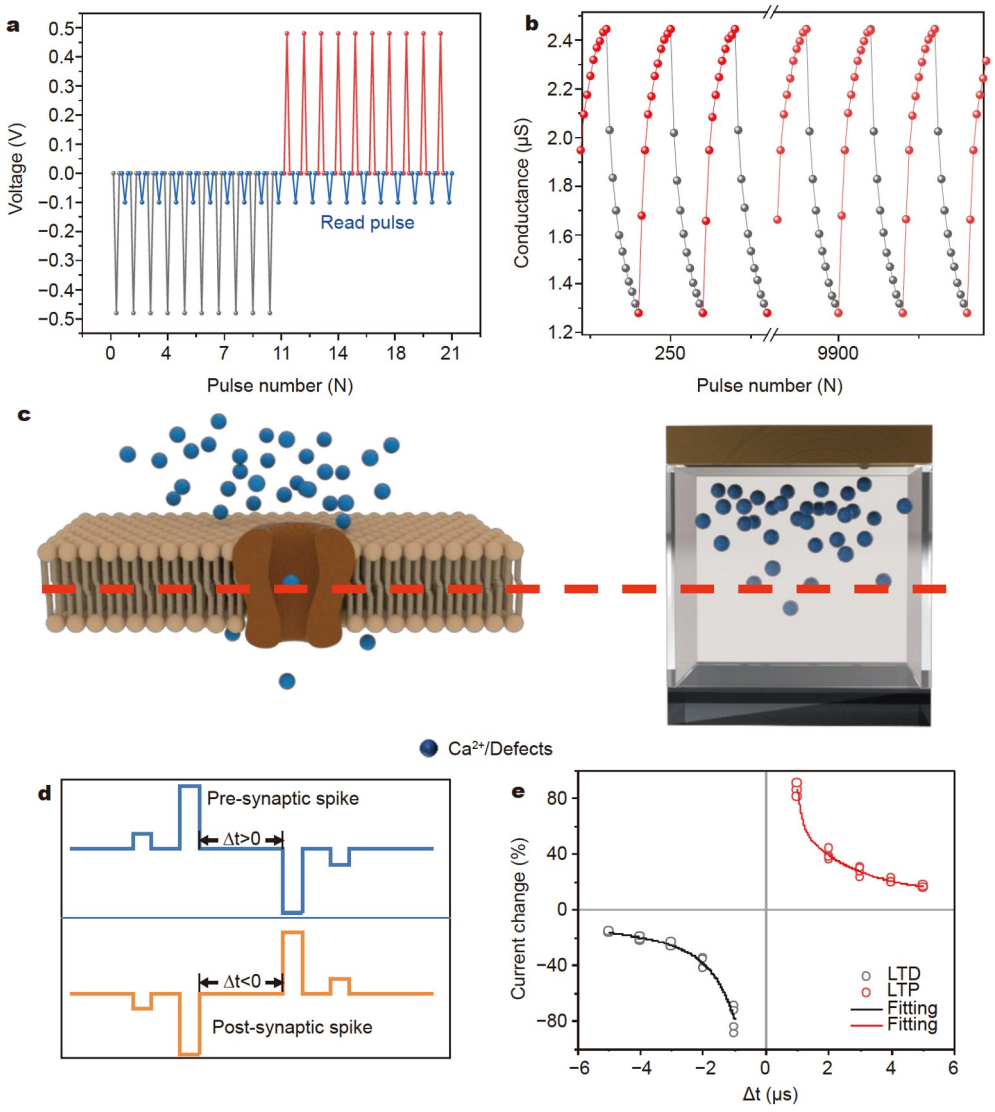

Figure 4 (a) Voltage sequence applied to the device and (b) conductivity value of the device under −0.1 V read pulse. The −0.48 and +0.48 V pulses will switch the device to the n-i-p and p-i-n directions, respectively. Pulse width: 0.5 ms, reading pulse width: 1 μs. Time interval between pulsed current and reading pulse: 0.25 ms. (c) Schematic diagram of biological synapses. (d) Pulses designed according to asymmetric Hebbian rules. (e) STDP measured under asymmetric Hebbian rules.

that the sign and amplitude of synaptic weight change are closely related to the relative times of presynaptic spike and post-synaptic spike. Take the most famous asymmetric STDP as an example, if the presynaptic spike arrives before the postsynaptic spike, it will lead to long-term potentiation (LTP) ($\Delta t > 0$, when $\Delta t = t_{post} - t_{pre}$). Conversely, it will cause long-term depression (LTD) ($\Delta t < 0$), which is determined by the change of conductivity of the device. The shapes of the front and rear spikes applied to the device are shown in Fig. 4d. The relationship between the change of reading current and Δt is shown in Fig. 4e.

In addition to STDP, SRDP is another important function of synapse [37], which has also been confirmed in our 2D-3D hybrid perovskite devices. Similar to biological synapses, 2D-3D hybrid perovskite devices show STP. When the repetition peak interval is long, the devices quickly return to the original state; when the repetition peak interval is short, the LTP of device conductivity changes. Fig. S10a, b show two pulse sequences applied to the device, including 20 pulsed currents with an amplitude of 0.3 V, width of 1 μs and interval of 4 ms or 4 s, respectively. The results show that the hysteresis current in the device comes from the reverse drift movement of ions in the p-i-n junction. When the pulse interval is small, the ions in the perovskite layer do not drift and diffuse to the equilibrium state before the arrival of the next pulsed current. The reflux current spike after each spike measured under zero bias explains the origin of STP functions of the device. In order to further study the influence of pulse on the regulation of device conductance, the effect of conductance regulation by changing the amplitude, width and interval of test pulse was tested (Fig. S11).

The organic-inorganic halide perovskite synaptic devices with switchable p-i-n structure caused by unintentional doping induced by ion migration are different from other reported artificial synapses based on conductive filament [38], ferroelectric tunnel junction [39], resistance change induced by ion movement [37], and phase change devices [40]. Considering

doping effect only requires atoms in a very small range, it consumes less energy due to the low activation energy of ion and vacancy migration in organic-inorganic halide perovskite materials, typically less than 0.5 eV [38]. Our devices are therefore more efficient than synaptic devices based on conductive filaments which requires the migrated ions to form conducting filaments. Due to the large pulsed current, the main energy consumption comes from electron tunneling in the polarization process. Using high amplitude and short duration pulses can significantly reduce energy consumption. As shown in Fig. 5a–c, the conductance of the device increases by 200% after a 1-V pulse current with a duration of 1 μs at a pre bias voltage of 0.1 V. The positive pulse current after the negative pulse is caused by the reverse discharge of the device. Although the processing speed of organic-inorganic halide perovskite synaptic devices is slower than that of inorganic-based memristors [39,40], which is five orders of magnitude faster than the calculation speed of biological synapse. Energy consumption (W) was calculated using the following formula:

$$W = Pt = U_{\text{pulse}} \times I_{\text{pulse}} \times t_{\text{width}}, \quad (1)$$

where P is the power consumption, U_{pulse} is the amplitude of pulse, I_{pulse} is the pulse current, and t_{width} is the width of pulse current. After the application of the pulsed current, the readout current increases from 0.06 to 0.2 μA, which corresponds to a 200% change in conductance. By putting the values in the formula, for a device with 0.07 cm^2 electrode size, an energy consumption of 35 pJ was obtained, which is similar to other reports as shown in Fig. 5d. However, the electrode size used in this study is more than seven times larger than that of the devices in the references. By calculating using the similar electrode size, an ultralow energy consumption of 1 fJ was estimated which is shown as the blue dot in Fig. 5d. Our devices are therefore highly more efficient than the existing memristors. The ultra-low energy consumption of our device makes it promising for the future application in neuromorphics.

CONCLUSION

In conclusion, in this work, the superior memristive performance of 2D-3D organic-inorganic halide perovskite films was studied, and the physical mechanism of resistance switching was discussed. It is proven that electron tunneling is the main conductive mechanism, and the movement and accumulation of defects lead to the change of conductivity. Moreover, our results show that ion vacancy-mediated 2D-3D organic-inorganic halide perovskite materials can function well as artificial synapse, with good STDP properties. In addition, compared with other reported oxides, chalcogenide 2D materials and ferroelectric materials, 2D-3D organic-inorganic halide perovskite materials have the advantages of low cost, solution processability, and low ion migration activation energy. The ultra-low energy consumption makes the devices promising candidates for the future neuromorphic applications. The performance of the device can be further improved by optimizing the types of defects by material engineering, controlling the number of defects by changing the film growth conditions, and using lithography technology to reduce the size of the device, and the

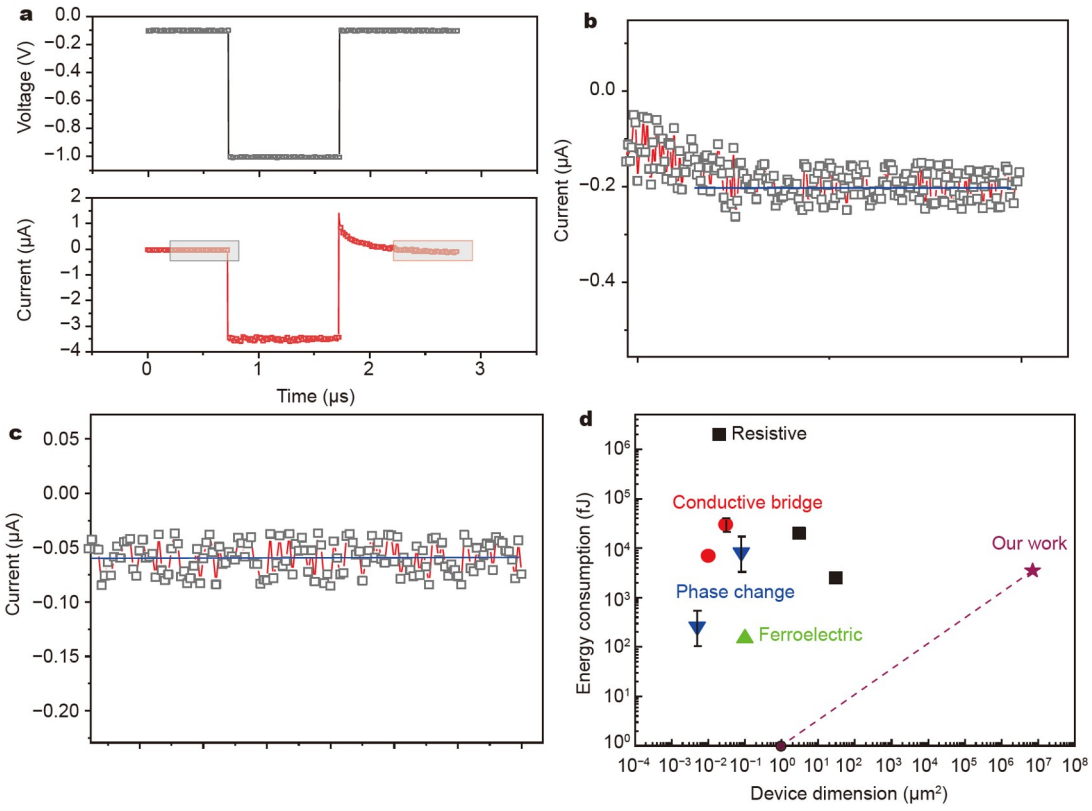

Figure 5 Energy consumption of the organic-inorganic halide perovskite synaptic devices. (a) Voltage pulse applied to the device (above) and the measured current (below). (b) Enlarged image in the black box in (a). (c) Enlarged image in the red box (a). (d) The energy consumption of our device is compared with the reported value in reference [41]. The purple dotted line indicates the energy consumption of a small-area device assuming that the polarization current is linear with the device area.

energy consumption of each event could be further reduced through device and material engineering.

Received 13 August 2022; accepted 8 November 2022; published online 17 February 2023

1 Shi Z, Guo J, Chen Y, *et al.* Lead-free organic-inorganic hybrid perovskites for photovoltaic applications: Recent advances and perspectives. Adv Mater, 2017, 29: 1605005
2 Jeon NJ, Noh JH, Yang WS, *et al.* Compositional engineering of perovskite materials for high-performance solar cells. Nature, 2015, 517: 476–480
3 Miyata A, Mitioglu A, Plochocka P, *et al.* Direct measurement of the exciton binding energy and effective masses for charge carriers in organic-inorganic tri-halide perovskites. Nat Phys, 2015, 11: 582–587
4 Stoumpos CC, Kanatzidis MG. Halide perovskites: Poor man's high-performance semiconductors. Adv Mater, 2016, 28: 5778–5793
5 Filip MR, Eperon GE, Snaith HJ, *et al.* Steric engineering of metal-halide perovskites with tunable optical band gaps. Nat Commun, 2014, 5: 5757
6 Walsh A, Stranks SD. Taking control of ion transport in halide perovskite solar cells. ACS Energy Lett, 2018, 3: 1983–1990
7 D'Innocenzo V, Srimath Kandada AR, De Bastiani M, *et al.* Tuning the light emission properties by band gap engineering in hybrid lead halide perovskite. J Am Chem Soc, 2014, 136: 17730–17733
8 Amat A, Mosconi E, Ronca E, *et al.* Cation-induced band-gap tuning in organohalide perovskites: Interplay of spin-orbit coupling and octahedra tilting. Nano Lett, 2014, 14: 3608–3616
9 Yin WJ, Shi T, Yan Y. Unusual defect physics in $CH_3NH_3PbI_3$ perovskite solar cell absorber. Appl Phys Lett, 2014, 104: 063903
10 Bi C, Shao Y, Yuan Y, *et al.* Understanding the formation and evolution of interdiffusion grown organolead halide perovskite thin films by thermal annealing. J Mater Chem A, 2014, 2: 18508–18514
11 Yuan Y, Huang J. Ion migration in organometal trihalide perovskite and its impact on photovoltaic efficiency and stability. Acc Chem Res, 2016, 49: 286–293
12 Leguy AMA, Frost JM, McMahon AP, *et al.* The dynamics of methylammonium ions in hybrid organic-inorganic perovskite solar cells. Nat Commun, 2015, 6: 7124
13 Eames C, Frost JM, Barnes PRF, *et al.* Ionic transport in hybrid lead iodide perovskite solar cells. Nat Commun, 2015, 6: 7497
14 Docampo P, Ball JM, Darwich M, *et al.* Efficient organometal trihalide perovskite planar-heterojunction solar cells on flexible polymer substrates. Nat Commun, 2013, 4: 2761
15 You J, Hong Z, Yang YM, *et al.* Low-temperature solution-processed perovskite solar cells with high efficiency and flexibility. ACS Nano, 2014, 8: 1674–1680
16 Kim BJ, Kim DH, Lee YY, *et al.* Highly efficient and bending durable perovskite solar cells: Toward a wearable power source. Energy Environ Sci, 2015, 8: 916–921
17 Liu T, Chen K, Hu Q, *et al.* Inverted perovskite solar cells: Progresses and perspectives. Adv Energy Mater, 2016, 6: 1600457
18 Zhao Y, Zhu K. Organic-inorganic hybrid lead halide perovskites for optoelectronic and electronic applications. Chem Soc Rev, 2016, 45: 655–689
19 Meloni S, Moehl T, Tress W, *et al.* Ionic polarization-induced current-voltage hysteresis in $CH_3NH_3PbX_3$ perovskite solar cells. Nat Commun, 2016, 7: 10334
20 Snaith HJ, Abate A, Ball JM, *et al.* Anomalous hysteresis in perovskite solar cells. J Phys Chem Lett, 2014, 5: 1511–1515
21 Wang Z, Lin Q, Chmiel FP, *et al.* Efficient ambient-air-stable solar cells with 2D-3D heterostructured butylammonium-caesium-formamidinium lead halide perovskites. Nat Energy, 2017, 2: 17135
22 Lin Y, Bai Y, Fang Y, *et al.* Enhanced thermal stability in perovskite solar cells by assembling 2D/3D stacking structures. J Phys Chem Lett, 2018, 9: 654–658
23 Stranks SD, Eperon GE, Grancini G, *et al.* Electron-hole diffusion lengths exceeding 1 micrometer in an organometal trihalide perovskite absorber. Science, 2013, 342: 341–344
24 Tress W, Marinova N, Moehl T, *et al.* Understanding the rate-dependent *J-V* hysteresis, slow time component, and aging in $CH_3NH_3PbI_3$ perovskite solar cells: The role of a compensated electric field. Energy Environ Sci, 2015, 8: 995–1004
25 Xing G, Mathews N, Lim SS, *et al.* Low-temperature solution-processed wavelength-tunable perovskites for lasing. Nat Mater, 2014, 13: 476–480
26 Dualeh A, Moehl T, Tétreault N, *et al.* Impedance spectroscopic analysis of lead iodide perovskite-sensitized solid-state solar cells. ACS Nano, 2014, 8: 362–373
27 Fan Z, Xiao J, Sun K, *et al.* Ferroelectricity of $CH_3NH_3PbI_3$ perovskite. J Phys Chem Lett, 2015, 6: 1155–1161
28 Brivio F, Walker AB, Walsh A. Structural and electronic properties of hybrid perovskites for high-efficiency thin-film photovoltaics from first-principles. APL Mater, 2013, 1: 042111
29 Walsh A, Scanlon DO, Chen S, *et al.* Self-regulation mechanism for charged point defects in hybrid halide perovskites. Angew Chem, 2015, 127: 1811–1814
30 Kim J, Lee SH, Lee JH, *et al.* The role of intrinsic defects in methylammonium lead iodide perovskite. J Phys Chem Lett, 2014, 5: 1312–1317
31 Yang JJ, Pickett MD, Li X, *et al.* Memristive switching mechanism for metal/oxide/metal nanodevices. Nat Nanotech, 2008, 3: 429–433
32 Xiao Z, Yuan Y, Shao Y, *et al.* Giant switchable photovoltaic effect in organometal trihalide perovskite devices. Nat Mater, 2015, 14: 193–198
33 Li Y, Zhong Y, Zhang J, *et al.* Activity-dependent synaptic plasticity of a chalcogenide electronic synapse for neuromorphic systems. Sci Rep, 2014, 4: 4906
34 Li Y, Zhong Y, Xu L, *et al.* Ultrafast synaptic events in a chalcogenide memristor. Sci Rep, 2013, 3: 1619
35 Abbott LF, Nelson SB. Synaptic plasticity: Taming the beast. Nat Neurosci, 2000, 3: 1178–1183
36 Shouval H. Spike timing dependent plasticity: A consequence of more fundamental learning rules. Front Comput Neurosci, 2010, 4: 19
37 Ohno T, Hasegawa T, Tsuruoka T, *et al.* Short-term plasticity and long-term potentiation mimicked in single inorganic synapses. Nat Mater, 2011, 10: 591–595
38 Waser R, Aono M. Nanoionics-based resistive switching memories. Nat Mater, 2007, 6: 833–840
39 Chanthbouala A, Garcia V, Cherifi RO, *et al.* A ferroelectric memristor. Nat Mater, 2012, 11: 860–864
40 Kuzum D, Jeyasingh RGD, Lee B, *et al.* Nanoelectronic programmable synapses based on phase change materials for brain-inspired computing. Nano Lett, 2012, 12: 2179–2186
41 Yuan Y, Chae J, Shao Y, *et al.* Photovoltaic switching mechanism in lateral structure hybrid perovskite solar cells. Adv Energy Mater, 2015, 5: 1500615

Acknowledgements This work was financially supported by the National Natural Science Foundation of China (61674050, 62004056, and 61874158), the Project of Distinguished Young of Hebei Province (A2018201231), the Support Program for the Top Young Talents of Hebei Province (70280011807), the Hundred Persons Plan of Hebei Province (E2018050004 and E2018050003), the Supporting Plan for 100 Excellent Innovative Talents in Colleges and Universities of Hebei Province (SLRC2019018), the Special Project of Strategic Leading Science and Technology of Chinese Academy of Sciences (XDB44000000-7), the Special Support Funds for National High Level Talents (041500120001), Hebei Basic Research Special Key Project (F2021201045), the Science and Technology Project of Hebei Education Department (QN2020178 and QN2021026), and Singapore Ministry of Education (AcRF TIER 2-MOE2019-T2-2-075).

Author contributions Sun K, Wang Q, Zhou L performed the experiments. Sun K conducted the fitting and data analysis. Sun K and Guo R prepared the original manuscript. All the authors contributed to the general discussion, review and editing. Guo R, Yan X, and Tay BK contributed to the conceptualization and supervision.

Conflict of interest The authors declare that they have no conflict of interest.

Supplementary information Supporting data are available in the online version of the paper.

Kaixuan Sun received his BSc degree in microelectronics science and engineering from the School of Physics and Optoelectronic Engineering, Xiangtan University, China in 2018, and ME degree in integrated circuit engineering from the College of Electronic and information Engineering at Hebei University. His current research interest is the field of memristor materials.

Beng Kang Tay is a pioneer in filtered catholic vacuum arc (FCVA) technology and has been working for many years in developing thin film materials especially in amorphous carbon, nanocomposites, graphene and carbon nanotubes. His current research interest includes the growth and application of 2D transition metal dichalcogenide materials and their heterostructures, the fabrication and characterization of nanostructures for field emission, thermal and high-frequency RF applications.

Xiaobing Yan is currently a professor at the College of Electronic and Information Engineering, Hebei University. He received his PhD degree from Nanjing University in 2011. From 2014 to 2016, he held a research fellowship at the National University of Singapore. His current research interest includes the study of novel flash memory, resistive memory, memristors and other novel electronic device integration and logic-controlled embedded circuit design for integration, and the study of memristor arrays for artificial neural networks.

用于神经形态学计算的低能耗、高稳定性2D-3D钙钛矿忆阻器

孙凯旋[1], 王庆瑞[2], 周龙[2], 王静娟[1], 常晶晶[2], 郭瑞[3*], Beng Kang Tay[3,4*], 闫小兵[1*]

摘要 近年来，有机-无机卤化物钙钛矿在忆阻器和人工突触器件等电子器件中的应用取得了快速进展. 由于其离子迁移特性和制造上的优势，有机-无机卤化物钙钛矿有望成为下一代计算设备的候选材料. 本文采用ITO/$FA_{1-y}MA_yPbI_{3-x}Cl_x$/$(PEA)_2PbI_4$/Au的叠层结构，研究了2D-3D有机-无机杂化钙钛矿忆阻器. 结果表明，这种新型忆阻器具有新颖的电阻开关特性，如扫描速率相关的电流开关特性、良好的电流-电压曲线重复性和超低能耗. 利用p-i-n结模型证实了缺陷调制电子隧穿机制，并证明了忆阻器件的电导状态由电极侧附近钙钛矿薄膜中的缺陷浓度决定. 除了良好的忆阻特性外，这种2D-3D钙钛矿型忆阻器还可以很好地用作人工突触，其内部缺陷运动可以真实地模拟生物突触中Ca^{2+}的流入和挤出. 此外，由于有机-无机卤化物钙钛矿中的可切换p-i-n结构，这种基于钙钛矿的人工突触具有超低功耗. 我们的发现展示了2D-3D钙钛矿忆阻器在未来神经形态计算系统中的巨大应用潜力.

